Transport properties in nontwist area-preserving maps

J. D. Szezech, Jr.,[1] I. L. Caldas,[1] S. R. Lopes,[2] R. L. Viana,[2] and P. J. Morrison[3]
[1]*Instituto de Física, Universidade de São Paulo, São Paulo, 05315-970 São Paulo, Brazil*
[2]*Departamento de Física, Universidade Federal do Paraná, Caixa Postal 19044, Curitiba, 81531-990 Paraná, Brazil*
[3]*Department of Physics and Institute for Fusion Studies, The University of Texas at Austin, Austin, Texas 78712, USA*

(Received 4 June 2009; accepted 22 September 2009; published online 23 October 2009)

Nontwist systems, common in the dynamical descriptions of fluids and plasmas, possess a shearless curve with a concomitant transport barrier that eliminates or reduces chaotic transport, even after its breakdown. In order to investigate the transport properties of nontwist systems, we analyze the barrier escape time and barrier transmissivity for the standard nontwist map, a paradigm of such systems. We interpret the sensitive dependence of these quantities upon map parameters by investigating chaotic orbit stickiness and the associated role played by the dominant crossing of stable and unstable manifolds. © *2009 American Institute of Physics*. [doi:10.1063/1.3247349]

Nonmonotonic flows with reverse shear are observed in many physical systems. Much previous research indicates that transport properties of such systems can be well described by area preserving maps. Many examples exist, e.g., in the fields of fluid mechanics and plasma physics; in particular, in models that describe zonal flows that occur in geophysics, atmospheric science, and fusion plasma physics. The standard nontwist map (SNM) is a well-known paradigm for investigating transport in reverse shear systems. The nonmonotonicity property of the SNM gives rise to transport barriers due to robust tori (invariant curves) that occur in zonal flows. These tori separate regions of the two-dimensional phase space. Moreover, the influence of these barriers on the transport remains even after the breakup of the tori. This phenomenon, i.e., the difficulty encountered in crossing broken barriers, is explained by examining the stickiness of orbits that occur in some regions of the map phase space. For a certain range of control parameters, these regions emerge near resonances. The presence of stickiness is closely related to the structure of the stable and unstable manifolds of hyperbolic orbits, becoming prevalent when the manifolds reconnect and change from a dominant homoclinic tangle to a combination that includes both homoclinic and heteroclinic tangles.

I. INTRODUCTION

A large number of systems of physical interest can be described by two-dimensional area-preserving maps that have the general form

$$J_{n+1} = J_n + f(\theta_n), \tag{1}$$

$$\theta_{n+1} = \theta_n - g(J_{n+1}), \tag{2}$$

where $J \in \mathbb{R}$ and $\theta \in (-\pi, \pi]$ are canonical variables and $f(\theta_n)$ is a period-2π function. Associated with all area-preserving maps are Hamiltonian flows, i.e., Hamiltonian ordinary differential equations with a smooth Hamiltonian function.[1] Area-preserving maps can also be obtained explicitly from a Hamiltonian function containing a δ-function that is periodic in time, such that J_m and θ_m are the action and angle values just before a delta kick occurring at integer time $n=m$. In the case of the map (1) and (2) such a Hamiltonian is given by (see, for example, Ref. 2)

$$H(J,\theta,n) = H_0(J) + H_1(\theta,t) = \int^J g(\xi)d\xi - \int^\theta f(\vartheta)d\vartheta \sum_{m=-\infty}^{\infty} \delta(n-m), \tag{3}$$

where we separate out an integrable part H_0 and a time-dependent perturbation H_1 that generically makes the system nonintegrable. Thus, (J,θ) are the action-angle variables for the unperturbed integrable system.

When $g(J)$ is a monotonically increasing or decreasing function of its argument, the map (1) and (2) fulfills the so-called twist condition for all (J_n, θ_n),

$$\left| \frac{\partial \theta_{n+1}(J_n,\theta_n)}{\partial J_n} \right| = |g'(J_{n+1})| \geq c > 0, \tag{4}$$

where c is a real number. The function $g'(J)$ is called the shear, where the prime denotes derivative with respect to argument. When $g(J)=J$ and $f(\theta)=K\sin\theta$ (such that the shear is equal to unity for all action values), Eqs. (1) and (2) become the standard map (SM), sometimes called the Chirikov–Taylor map,[3]

$$J_{n+1} = J_n + K\sin(\theta_n), \tag{5}$$

$$\theta_{n+1} = \theta_n - J_{n+1}, \tag{6}$$

where $K>0$ measures the intensity of the perturbation.

In this work we are interested in the case where $g(J)$ is nonmonotonic and may have a countable number of extrema. Let $J=J_S$ indicate one such local extremum. Linearizing $g(J)$ in the vicinity of J_S gives

$$g(J) \approx g(J_S) + \tfrac{1}{2}g''(J_S)(J - J_S)^2. \tag{7}$$

Since by hypothesis $g'(J_S)=0$, we call J_S the shearless action, and the set $\{(\theta,J)\,|-\pi<\theta\leq\pi, J=J_S\}$ is the corresponding shearless curve. It should be noted that since the twist condition (4) is violated at J_S, a map with g given by Eq. (7) corresponds to a nontwist map.

Since $g(J_S)$ is a constant, it can be set equal to zero without loss of generality. Introducing the normalized variables $x=\theta/2\pi$ and $y=J/J_S$ and defining

$$a := \frac{1}{4\pi}g''(J_S), \quad f(\theta) := -bJ_S \sin(\theta), \tag{8}$$

the map (1) and (2) becomes the so-called SNM, as given in Ref. 4 (and studied in detail in Refs. 5 and 6),

$$x_{n+1} = x_n + a(1 - y_{n+1}^2), \tag{9}$$

$$y_{n+1} = y_n - b\,\sin(2\pi x_n), \tag{10}$$

where $x\in[-1/2,+1/2)$ and $y\in\mathbb{R}$. If J_S is a local minimum then $a>0$. We usually limit the investigation to the range $a\in(0,1)$, whereas b may take on any real value. Using Eq. (3), the Hamiltonian with kicks corresponding to the map (9) and (10) (see Ref. 4) is

$$H(x,y,n) = H_0(y) + H_1(x,t)$$
$$= ay\left(1 - \frac{y^2}{3}\right) - \frac{b}{2\pi}\cos(2\pi x)\sum_{m=-\infty}^{\infty}\delta(n-m). \tag{11}$$

Nontwist maps appear in many physical problems, in particular, when modeling continuous systems that describe features of fluids and plasmas. One application of nontwist maps is to the problem of passive advection of a tracer particle in a two-dimensional incompressible flow. The time evolution of a Lagrangian trajectory $(x(t),y(t))$ of an advected passive scalar is described by canonical equations, where a stream function that corresponds to an equilibrium state plays the role of the integrable Hamiltonian H_0. Nonmonotonicity occurs when the flow shear reverses sign along some shearless curve, as is the case for zonal flows of geophysical and atmospheric interest.[4,7] One example is the Bickley jet for which the velocity profiles are symmetric with a single maximum.

Perturbations of this equilibrium configuration corresponding to H_1 of Eq. (11) may come from traveling waves such as Rossby waves superimposed on the equilibrium shear flow. Such waves play an important role in zonal sheared flows that occur in both oceans and atmospheres, like the Gulf stream and the jet current.[7] Due to the nonintegrable nature of the combined Hamiltonian, chaotic behavior occurs for the advected particle trajectories, even though the fluid velocity field need not be chaotic at all.

Another example is the description of the magnetic field lines in toroidal fusion devices like the tokamak[8] and the reversed field pinch.[9] The magnetic field line equations for such devices are known to have Hamiltonian form with x and y corresponding to the angular and radial positions, respectively, of the intersection between a field line and a surface of section in the phase space (see, for example, Refs. 10 and 11). The field line itself can be parametrized by an ignorable coordinate, which plays the role of time in the canonical equations.

The equilibrium magnetic field line configuration represents an integrable Hamiltonian system in the sense that magnetic field lines lie on nested surfaces with $H_0=$const. In such systems, the function $g(y)$ describes the so-called safety factor, a quantity related with the current density of the plasma discharge in the toroidal device. In tokamaks, nonmonotonic forms of $g(y)$ may result from hollow toroidal current profiles, which can be obtained by many experimental techniques and are related with enhanced confinement; for example, this happens when neutral beam injection is applied as a noninductive current drive.[12] It was suggested in Refs. 13 and 14 (see also Ref. 11) that enhanced confinement should occur because of robust tori associated with the shearless curve. The shearless curve here occurs at the radial position where the magnetic shear $g'(y)$ changes sign.

The perturbing Hamiltonian H_1 in this problem results from any or all of the following: (i) the addition of internal or external resonant magnetic fields usually created by externally applied electric currents, like in divertors and ergodic magnetic limiters; (ii) error fields due to coil misalignments; and (iii) plasma instabilities.[15,16] The successive piercings of a magnetic field line with the surface of section for these effects are modeled by the periodic delta function in H_1.

Yet another problem in which the SNM appears is in the description of the $\mathbf{E}\times\mathbf{B}$ drift motion of charged particles in a magnetized plasma under the action of a time-periodic electric field from an electrostatic wave.[14,17] The source of nontwist behavior in this case is a nonmonotonic radial electric field profile that may show up in the plasma edge of a toroidal plasma device (such as the tokamak) during the high confinement (or H-mode) regime.[18,19] The relevant transport properties here occur in the plane perpendicular to the magnetic field and are also related to the loss of particles and energy through collisions with the device wall[20,21] and other obstacles like divertors.[22]

Since the SNM describes a nonintegrable system, chaotic orbits occur with any nonzero perturbation, and a great deal of information has been obtained from a thorough analysis of the (a,b) parameter plane.[5,6,23,24] A physically meaningful question is to what extent do the peculiar characteristics of the SNM affect the diffusion (in action) that occurs in the chaotic orbits. In the applications of SNM listed above, the formation of a transport barrier located in the neighborhood of the shearless curve has been observed. This barrier decreases the action transport rates and hinders diffusion. For example, in toroidal plasma devices with magnetic field line structure described by the SNM, this transport barrier can explain why nonmonotonic safety factor profiles improve the plasma confinement time, as was suggested in Refs. 13 and 14. Since diffusive radial transport decreases, fewer plasma particles are expected to be lost due to collisions with the containment walls, as well as related processes of energy release.

Many dynamical aspects of nontwist maps are radically different from the better-known twist maps, for which the diffusion in action space is reasonably well understood. This

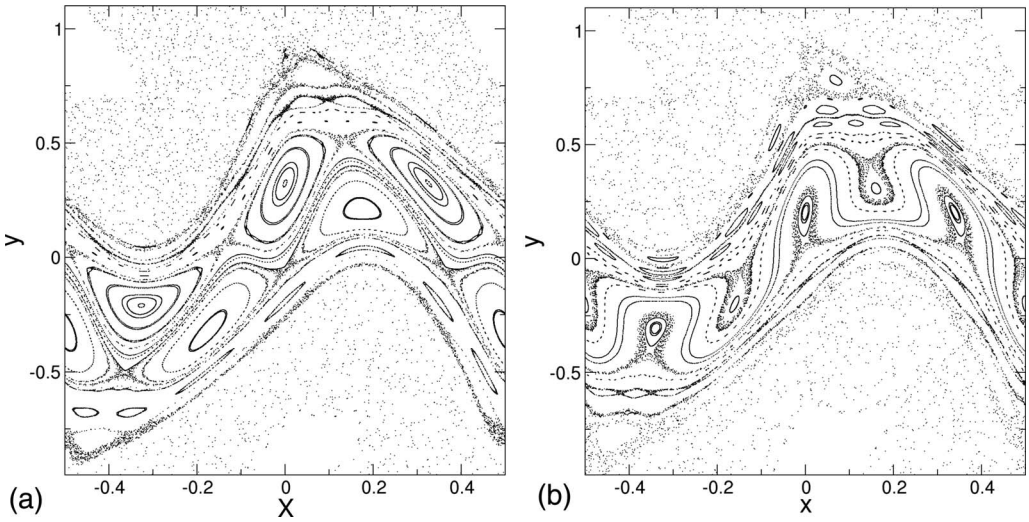

FIG. 1. Surfaces of section for the SNM for $b=0.6$ and (a) $a=0.364$; (b) $a=0.354$.

justifies the present effort dedicated to understanding the transport properties of nontwist maps, of which the SNM is the paradigm due to its simplicity. Our goal in this paper is to discuss the effect of stickiness and the role played by the crossing of invariant manifolds on the transport properties of the SNM.

Although far from the shearless curve stickiness, manifold crossing, and the related transport may be considered similar to what we observe in twist maps, for the SNM, however, the presence of the shearless region changes dramatically the scenario due to arising of bifurcations which substantially increase the stickiness in that region. This reflects in the transport phenomena in the shearless region, like the escape times and transmissivity, which are different (by orders of magnitude) from the rest of the phase space. In this sense, the SNM is hence stickier than twist maps, which causes the reported persistence of the partial transport barrier for a large variation in control parameters.

This paper is organized as follows. In Sec. II we review some facts about reconnection of separatrices and barrier destruction for the SNM. Section III deals with some transport properties of the SNM. Section IV aims to interpret these properties in terms of the invariant manifold structure near the barrier. Our conclusions are left to Sec. V.

II. RECONNECTION AND BARRIER DESTRUCTION

As noted in Sec. I, the SNM plays a role for nontwist systems similar to that played by the SM for twist systems.[5,6,23] However, proofs of many important results of Hamiltonian nonlinear dynamics, such as the Kolmogorov–Arnold–Moser (KAM) theorem, the Poincaré–Birkhoff theorem, and Aubry–Mather theory, may require the twist condition.[2,25,26] Hence, many phenomena typical of twist maps do not occur in nontwist maps, and new features may also occur. As an example, for the SM the interaction between adjacent periodic islands produces the merging of their chaotic separatrix layers and the chaoticization of a region formerly comprising the islands. In the SNM, however, this may not be true in the vicinity of the shearless curve (see, for example, Ref. 23). Adjacent orbits may actually suffer a reconnection process and eventually coalesce into a different structure without generating a large-scale chaotic region in its place.

If the parameter a is small enough, then on each side of the shearless curve there develops a chain of period-p islands. The behavior is different according to the period p of the orbit related with the island.[23] If the orbits have even p, then the orbits on each side of the shearless curve have the same stability type, i.e., if one is a center (saddle) the other is a also a center (saddle). However, if p is odd, then the stability types are different on both sides of the shearless curve, as exemplified by Fig. 1(a), where there are two period-3 orbits, one on each side of the shearless curve that has different stability types. At $x=-0.5$, for example, the orbit below the curve is a center, whereas it is a saddle above the curve, and so on.

As the parameter a is changed, the two island chains approach each other in such a way that the hyperbolic manifolds of the up and down orbits connect (not shown in Fig. 1), eventually leaving each orbit with a homoclinic and a heteroclinic manifold. In the region between the orbits, we observe the formation of new periodic orbit invariant curves, not predicted by KAM theory, since these orbits would not exist if the perturbation were zero [Fig. 1(b)]. Such non-KAM tori, also called meanders, are not graphs over the x-axis.[23,27] Accordingly, we call the region occupied by the collection of meanders the meandering region, which appears in the neighborhood of the shearless curve.

The meandering region has periodic orbits that suffer reconnection, such that the same picture will appear locally in many places. This second-order reconnection leads to second-order meanders and so on. If the perturbation (represented here by the parameter a) is large enough, the meandering region becomes increasingly dominated by chaotic orbits, until a single meander survives. This last meander is a transport barrier in the sense that orbits that originate from points above (below) the barrier are kept above (below) the barrier for all future times. We illustrate this point in Fig.

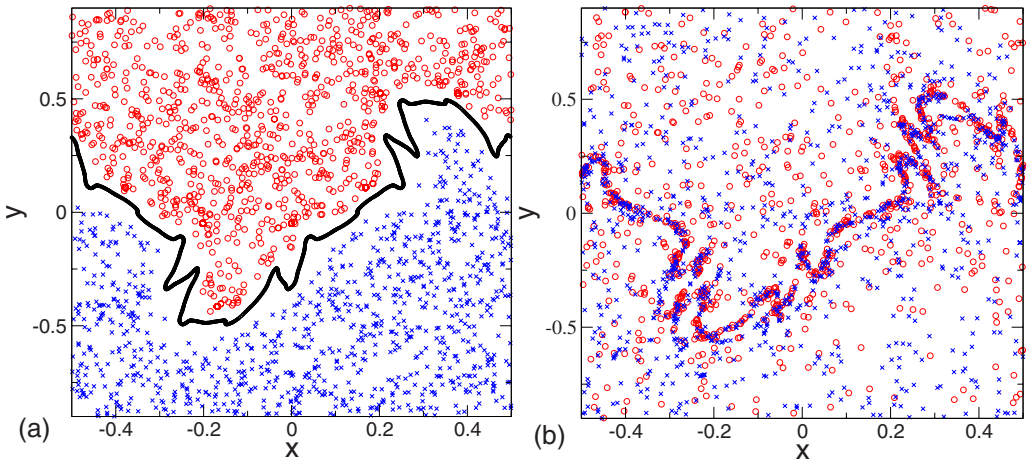

FIG. 2. (Color online) Phase portraits of the SNM for $b=0.6$ and (a) $a=0.8000$ and (b) $a=0.8063$. The red (blue) points represent orbits whose initial conditions were chosen above (below) the last meander, depicted as a black line in (a).

2(a) by plotting such orbits in different colors. Observe that there is no mixing of colors even for large times. A slight increase in the perturbation will destroy the barrier, leading to large scale diffusion in the y-direction [see Fig. 2(b)]. In the following, we will investigate the transport properties in this direction after the barrier has been broken and investigate the role played by the crossing of the invariant manifolds of periodic orbits embedded in the chaotic region.

III. DIFFUSION AND ESCAPE OF TRAJECTORIES

Unlike the SM, which is often assumed to be periodic in both the x- and y-directions, the y-direction of the SNM is unbounded and this excludes, for example, the presence of accelerator modes that enhance the transport rates. Moreover, the unboundedness of y leads to other differences between the diffusion properties of the SM and the SNM. Orbits of the SNM can diffuse to both plus and minus infinities. Before the barrier breakup an orbit that has an initial condition above (below) the barrier will diffuse to plus (minus) infinity [Fig. 2(a)]. After the barrier destruction the asymptotic state depends sensitively on the initial condition, and trajectories may cross the barrier remnants and penetrate a formerly forbidden region of the phase space [Fig. 2(b)].

In order to investigate the dependence of the diffusion properties on initial conditions and map parameters chosen near the values for barrier destruction, we computed the escape time of orbits by the following numerical experiment. For given values of the parameters (a,b) we tested a large number of initial points $N_P=2\times10^6$ placed on a regularly spaced grid in the square $[-0.5,0.5]\times[-0.9,0.9]$. These intervals were chosen to ensure a reasonable sampling of chaotic orbits with relevant islands located mainly near the barrier remnants, as depicted in Fig. 2(b), for instance. Each initial condition was iterated until the corresponding orbit crossed either one of two reference boundaries $\{(x,y)|-0.5<x_B<0.5$ and $y_B=\pm2.0\}$. The values of $\pm y_B$ were chosen rather arbitrarily and, since there are no islands of noticeable size above them, we expect the results do not depend in a significant way upon these values. The escape time $\tau_{\rm esc}$ is the time it takes for an orbit to reach the boundary lines, and it is generally different for different initial conditions. Hence, we computed the average escape time $\bar{\tau}_{\rm esc}$. Figure 3(a) shows the average escape time as a sweeps an interval of values immediately below and above the critical value for barrier breakup. We observe a strong dependence on a with peaks in the escape time after barrier breakup, such as for $a\approx0.8049$ and 0.8063. This indicates the presence of some kind of trapping mechanism that hinders diffusion.

Another numerical experiment was performed to investigate the diffusion across the barrier after its breakup. We placed $N_P=4.5\times10^6$ initial conditions on the line $\{(x,y)|-0.5<x_B<0.5$ and $y=1.0\}$ and iterated the resulting orbit $T=2.0\times10^6$ times. The *transmissivity*, defined as the fraction of orbits that cross the transport barrier in this given time, was calculated. The results [Fig. 3(b)] indicate that the transmissivity becomes nonzero at $a_{CR}\approx0.8039$, which is an estimate of the a-parameter value for the barrier breakup. Moreover, for $a\gtrsim a_{CR}$ the transmissivity depends on a in a nonmonotonic fashion, exhibiting an overall peak at $a\approx0.8055$.

The fine details of the dependence of the escape time on the initial conditions can be clarified by examination of Figs.

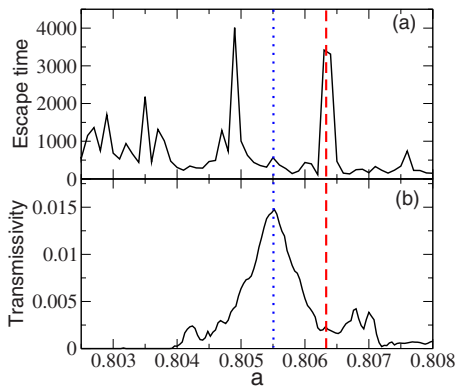

FIG. 3. (Color online) (a) Mean escape time and (b) transmissivity of the SNM with $b=0.6$ and variable a. The blue dotted line indicates an a-value of fast escape and large transmissivity, while the red dashed line indicates an a-value with an effective barrier in that the escape time is long and the transmissivity is low.

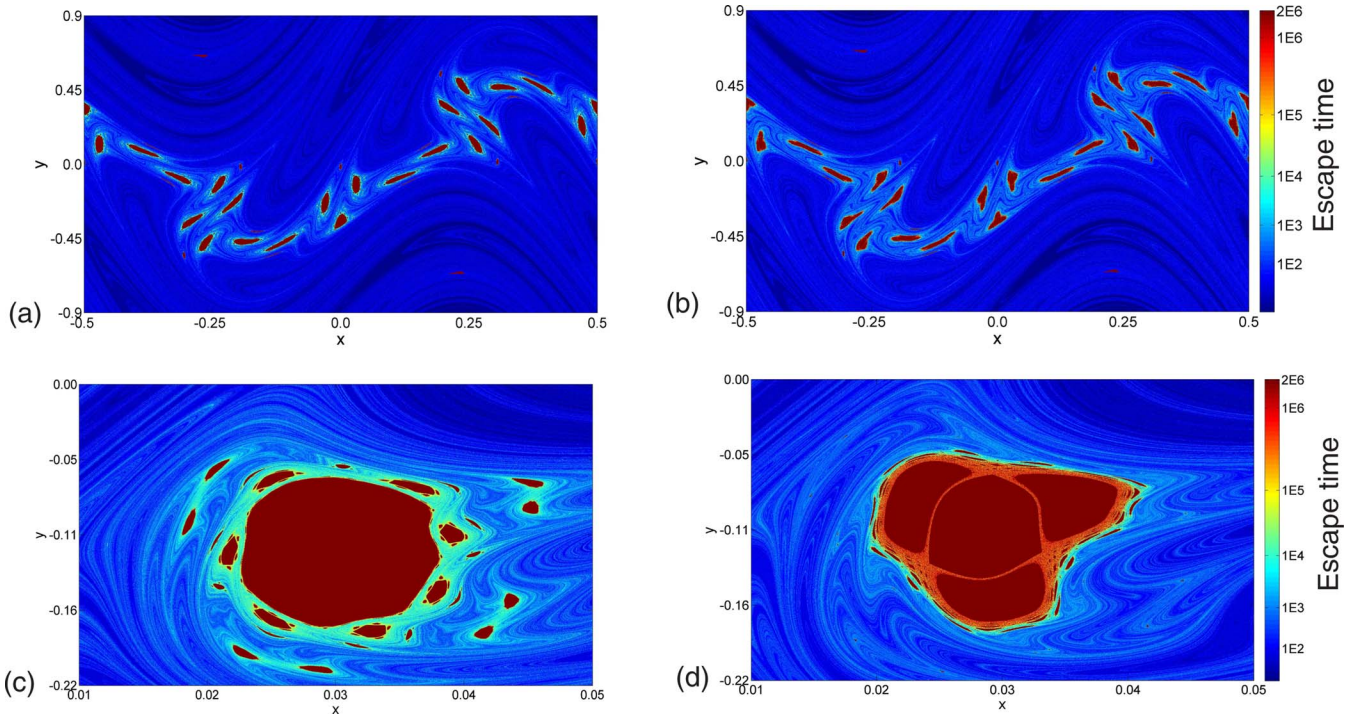

FIG. 4. (Color online) Escape time (in color scale) for different initial conditions for the SNM with $b=0.6$ and (a) $a=0.805\,52$; (b) $a=0.806\,30$, corresponding to the blue dotted and the red dashed lines in Fig. 3, respectively. (c) Magnification of a region of (a) near a periodic orbit. (d) Magnification of a region of (b) near a periodic orbit.

4(a) and 4(b), for which we chose two values of a: one that corresponds to small escape time and large transmissivity (blue dotted line in Fig. 3) and one that corresponds to large escape time and small transmissivity (red dashed line in Fig. 3). In both cases the barrier has been broken, but there remain island chains with centers belonging to upper and lower period-11 orbits. Points inside these islands evidently do not diffuse, but the orbits adjacent to them, although subject to diffusion, spend more time lingering than most of the other points. This can be seen in Fig. 4(d), where we depict a magnification of the vicinity of a selected island belonging to the lower chain, in which a second-order "period-3 chain" has been formed (actually with period 3×11). For such period-3 phenomena, it has been shown that generically there exist shearless curves,[28] and such shearless curves have been found in perturbed magnetic configurations with nonmonotonic winding number profiles (see, for example, Ref. 29). On the other hand, Fig. 4(c), which is a magnification of Fig. 4(a), does not show such period-3 chain.

This strong dependence on initial conditions and associated lingering adjacent to island chains, also called *stickiness*, has been extensively studied in twist systems (see, for example, Ref. 30). The chaotic orbit in the vicinity of the period-3 chain spends a large amount of time encircling it, shadowing in a sense the nearby periodic orbits. After experiencing this trapping regime, the orbit is free to diffuse until it approaches the vicinity of another periodic orbit where it may become trapped again, and so on. When transport behaves like this, alternating between diffusive and trapped motion, one expects the transport to be anomalous and more aptly described by a Lévy flight[30,31] scenario.

An illustration of stickiness is provided by Fig. 5(a), where we plot the phase portrait for a single initial condition chosen in the vicinity of the same period-3 chain displayed in Fig. 4(d). The concentration of black points near the island separatrix results from the lingering of the orbit in this region. This period of time can be determined by computing the finite-time Lyapunov exponent for the respective orbit.

Finite-time Lyapunov exponents quantify local rates of divergence or contraction of the phase space and have been successfully used to describe stickiness in the SM.[32] Let $\mathbf{M}(x,y)$ be the SNM given by Eqs. (9) and (10), and n be a positive integer, such that $\mathbf{DM}^n(x_0,y_0)$ denotes the Jacobian matrix of the n-times iterated map evaluated at the point (x_0,y_0). The eigenvalues of $\mathbf{DM}^n(x_0,y_0)$ are $\xi_1(x_0,y_0,n) \geq \xi_2(x_0,y_0,n)$. The kth time-n Lyapunov exponent for a chaotic orbit originating at the point (x_0,y_0) is

$$\lambda_k(x_0,y_0,n) = \frac{1}{n}\ln(\|\mathbf{DF}^n(x_0,y_0)\mathbf{u}_k\|), \quad k=1,2, \tag{12}$$

where $\mathbf{u}_k$ is the eigenvector corresponding to the eigenvalue ξ_k. In Fig. 5(b) we follow the time evolution of the time-100 maximal Lyapunov exponent for the same initial condition used to draw the phase portrait of Fig. 5(a). The trapping behavior of this orbit lasts for $T\approx2\times10^5$ iterations, corresponding to the small-amplitude fluctuations of $\lambda_1(100)$ near zero. Afterward, when the orbit is released and wanders through the available chaotic region, these fluctuations increase in amplitude by a factor of 10, with an average that is asymptotically equal to the infinite-time Lyapunov exponent of ~0.07 of the corresponding chaotic orbit.

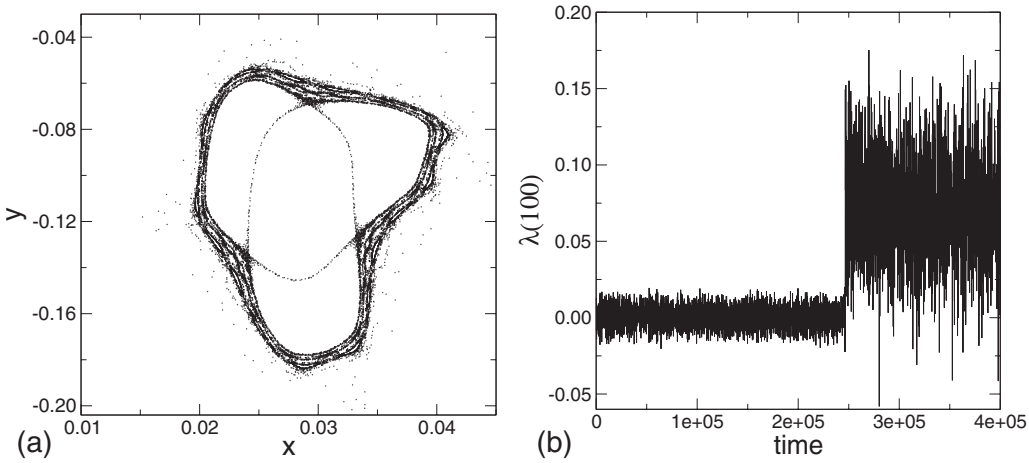

FIG. 5. (a) Phase portrait of a single chaotic orbit in the vicinity of the period-3 chain depicted in Fig. 4(d). (b) Time evolution of the time-100 maximal Lyapunov exponent for this chaotic orbit.

The statistical distribution of dynamically relevant quantities, such as exit times, return times, recurrences, etc., in the presence of stickiness possesses power-law tails, a characteristic feature of Lévy flights.[30] We verified this by computing numerical approximations of the probability distribution function for the escape times $P(\tau_{\rm esc})$ obtained from a large number of initial conditions. In Fig. 6 we show these distributions for parameters corresponding to Figs. 4(a) and 4(b). When the parameter a is such that the average escape time is small (blue dashed curve) the distribution can be fit to the power-law $P(\tau_{\rm esc}) \sim \tau_{\rm esc}^{-\alpha}$ with $\alpha = 1.93$. When the parameter a corresponds to a large average escape time (red curve), the effect of stickiness is to add a power-law tail with an exponent of -0.83.

Another quantitative characterization of stickiness was obtained by choosing $N_I = 5000$ initial conditions uniformly distributed within a small region at different locations adjacent to the period-3 chain belonging to the barrier remnant. We chose a parameter value for which the escape time is large, corresponding to the peak indicated by the red dashed line in Fig. 3(a). We iterated these initial conditions and, for each discrete time n, we computed the fraction of the corresponding orbits that cross the reference boundaries at $\{(x,y) | -0.5 < x_B < 0.5 \quad \text{and} \quad y_B = \pm 2.0\}$. Since all initial conditions were chosen in the chaotic region, this fraction is expected to vanish for large times, but stickiness can retard this decay. In Fig. 7(a) the time evolution of this fraction is followed for initial conditions chosen in the three distinct rectangles indicated in Fig. 7(b). These rectangles correspond to regions increasingly further away from the immediate vicinity of the period-3 chain and, accordingly, the fraction decays with different rates for them. In other words, the closer the initial conditions are to the period-3 chain boundary, the slower is the decay of the fraction of remaining trajectories caused by stickiness.

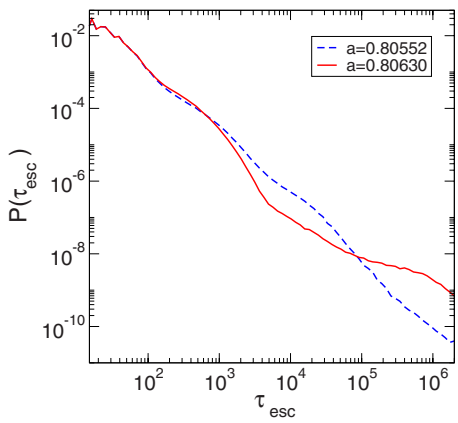

FIG. 6. (Color online) Probability distribution functions of the escape times for the SNM with $b = 0.6$ and different values of a.

Stickiness makes diffusion anomalous in the sense that the mean square deviation (in the y-direction) of orbits scales with time as a power law, instead of being directly proportional to n, as is the case for Gaussian (normal) diffusion

$$\sigma^2 = 2Dn^{\nu}, \tag{13}$$

where $\nu < 1$ (>1) corresponds to subdiffusion (superdiffusion) and $\nu = 1$ corresponds to Gaussian diffusion. In Fig. 8 we plot the diffusion coefficient as a function of time, computed from 5000 initial conditions chosen within the same rectangular boxes depicted in Fig. 7(b).

The orbits in box A, which is very close to the period-3 chain boundary, linger for a long time with a variance not showing significant increase, a behavior corresponding to no diffusion at all, which is indicative of stickiness. On the other hand, as we move away from this boundary, this lingering time decreases, and Gaussian diffusion sets in earlier, as expected for a region free of stickiness. For large times, the diffusion coefficient thus approaches the quasilinear value[3]

$$D_{\rm QL} = \frac{b^2}{4} = \frac{(0.6)^2}{4} = 0.09, \tag{14}$$

which is the same value as that for the SM, since the y-dynamics is the same. Note that between these two regimes of lingering and Gaussian diffusion the transport is superdiffusive; this is a consequence of fast channel escape, which will be discussed in the next section.

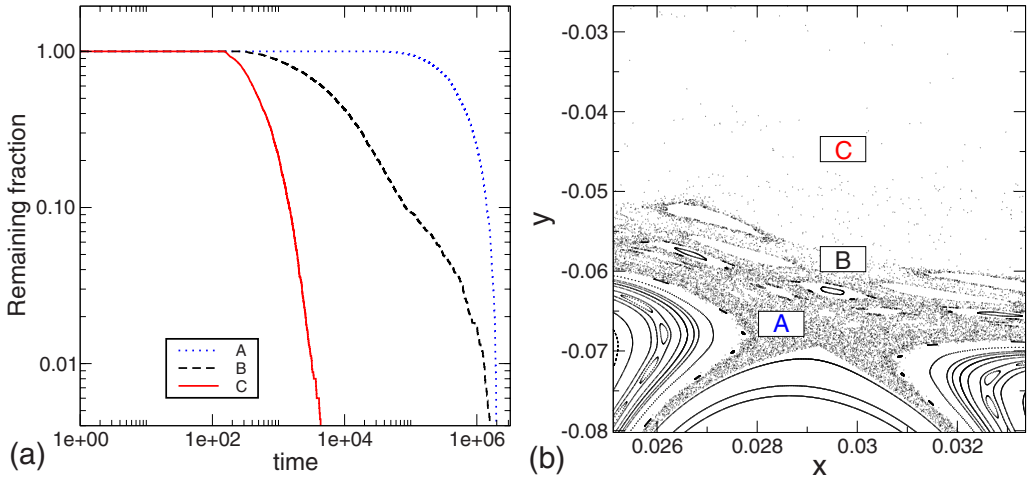

FIG. 7. (Color online) (a) Fraction of remaining trajectories for the SNM with $b=0.6$, $a=0.806\ 30$ and initial conditions chosen within the rectangles indicated in (b).

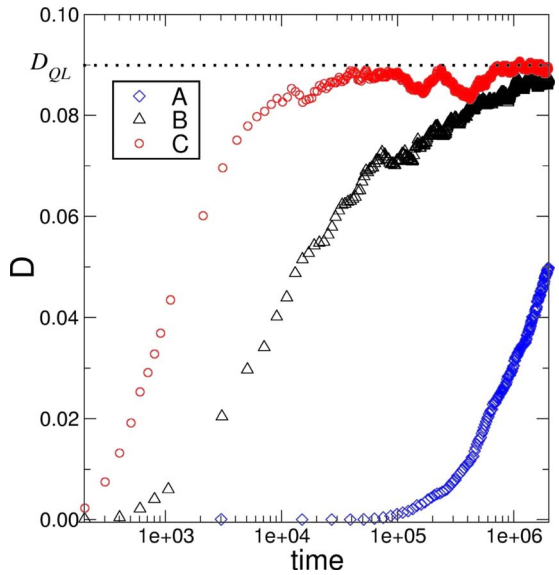

FIG. 8. (Color online) Diffusion coefficient as a function of time for initial conditions chosen within the same rectangular boxes depicted in Fig. 7(b).

IV. INVARIANT MANIFOLDS AND ESCAPE CHANNELS

From Sec. III, it is clear that remnants of barrier breakdown and associated stickiness are intimately associated with the nonuniform transport of chaotic orbits in the SNM. In fact, the basic mechanism for chaos arises from the crossing of stable and unstable manifolds of hyperbolic orbits and the horseshoe map structure (see, for example, Ref. 33) that results. Therefore, it is not surprising that alteration in this manifold structure has been associated with enhanced transport both in twist and nontwist maps.[21,34,35] A mechanism for such enhanced transport is described here.

Figure 9 shows, using different colors, the stable and unstable invariant manifolds of two hyperbolic orbits embedded in the chaotic regions of the upper and lower chains forming the transport barrier remnants described in Sec. III. Yellow and blue curves represent the stable and unstable manifolds of the upper (outer relative to a period-3 chain element) hyperbolic orbit, respectively, while green and red

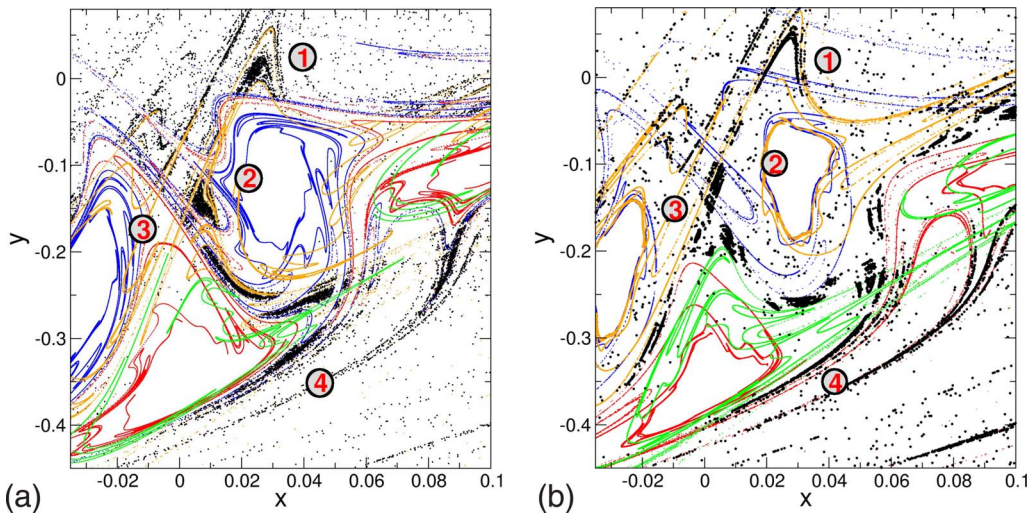

FIG. 9. (Color online) Stable and unstable manifolds of hyperbolic points within a chaotic region of the SNM with $b=0.6$ and (a) $a=0.805\ 52$; (b) $a=0.806\ 30$, corresponding to the blue dotted and the red dashed lines of Fig. 3, respectively.

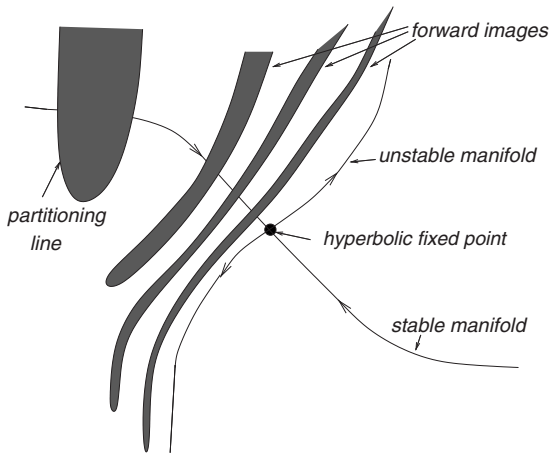

FIG. 10. Schematic of the formation of escape channels.

are those for the lower hyperbolic orbit. The unstable manifolds in both cases are homoclinic to the hyperbolic orbits, respectively. Figures 9(a) and 9(b) were drawn for values of a corresponding to the blue dotted and the red dashed lines of Fig. 3, respectively. The manifold branches were numerically obtained by selecting a set of initial conditions that accumulated on the stable manifold.[36] This method has been called the "sprinkler method." One of its advantages is that we do not need to specify the exact position of the hyperbolic orbits from which the invariant manifolds emanate.

In both cases the manifold branches intersect transversely forming a complex structure. The striations displayed by the manifold branches are closely related with escape channels that are revealed by a closer look at Fig. 4. The deep blue regions there, indicating moderately small escape times, are intermixed with the light blue regions indicating very small escape times. The deep and light blue regions form incursive fingers that act as escape channels, through which chaotic orbits diffuse in the y-direction.[37]

The mechanism underlying the escape channel formation is schematically illustrated in Fig. 10 of Ref. 37. Let P be a hyperbolic point embedded in the chaotic region with its stable and unstable subspaces denoted by $E_s(P)$ and $E_u(P)$, respectively. The eigenvalues of the tangent map **DF** corresponding to $E_s(P)$ and $E_u(P)$ are real and have moduli greater than and less than unity, respectively, with their product being equal to unity. These subspaces are tangent to the stable $W_s(P)$ and unstable $W_u(P)$ manifolds at P. Let A be a set of initial conditions whose boundary, a partitioning line, is an invariant manifold lobe that crosses the stable manifold of P. The forward images of this region under the SNM, $\mathbf{F}^m(A)$, $m=1,2,3,\ldots$, also cross the stable manifold as depicted in the figure. These forward images approach the hyperbolic point P yielding fingerlike regions that shrink along the direction of the stable manifold $W_s(P)$, with a rate equal to the corresponding eigenvalue of the tangent map in P. Since the map is area preserving, these fingerlike regions will also elongate along the direction of the unstable manifold $W_u(P)$. As time goes to infinity, the fingers tend to accumulate on the unstable manifold forming long winding spaghettilike striations. This is a rough description of the basic horseshoe map mechanism of Hamiltonian chaos. Stickiness is explained by the high concentration of manifold striations in the immediate vicinity of an island boundary, as can be observed in Figs. 9(a) and 9(b), which is a magnification of the period-3 chain near the outermost closed torus of the island remnants after the barrier breakdown.

The nonuniformity in the invariant manifold concentration also explains the different transmissivities observed in Figs. 9(a) and 9(b). The case of high transmissivity [Fig. 9(a)] displays many crossings between manifold branches associated with hyperbolic points both above and below the barrier remnant. For the up hyperbolic orbit we have the conventional *intracrossing* and associated homoclinic tangle of the yellow and the blue invariant manifolds, while for the down we have the intracrossing of the red and green. However, we also see *intercrossings* between stable and unstable manifolds of the up and down orbits, giving rise to a heteroclinic tangle between the up and down hyperbolic orbits. For example, careful examination of the figure shows that the up yellow stable manifold crosses the down red unstable manifold (as well as the up blue unstable manifold). Thus, there are crossing points of both homoclinic and heteroclinic types, i.e., under iteration there are points that remain on each of the invariant stable manifolds and attract to the up and down hyperbolic points. Since sets of initial conditions tend to accumulate along the manifold thread obtained from such crossings, because of these dominant crossings we expect orbits to escape more rapidly across the barrier remnant. In terms of Fig. 9(a) we see that for most orbits starting in region 1, forward images are first mapped into region 2 and later into region 4. Only relatively few orbits starting from 1 go to region 3.

For the small transmissivity case [Fig. 9(b)], we observe again dominant intracrossings above and below the barrier remnant, but the intercrossings are not evident. Yellow and blue are seen to cross, and red and green are seen to cross, but unlike in Fig. 9(a) crossings of red with yellow, for e.g., are not seen. In terms of Fig. 9(b) most orbits starting in 1 have forward images mapped into region 2 and later into 3. Comparatively few orbits starting from 1 go to region 4. In this case the transmissivity is comparatively low and the barrier remnant acts as an effective barrier if the characteristic time it takes for a typical orbit to cross the barrier is much greater than the time scale of interest (such as the duration of an experiment).

This difference between the transmissivities in Figs. 9(a) and 9(b) is schematically depicted in Fig. 11. When the barrier transmissivity is high, the dominant invariant manifolds have intercrossings [with up labeled by A and down by B in Fig. 11(a)]. If the transmissivity is low, the intracrossings of invariant manifolds dominate [Fig. 11(b)]. Such a scenario could be understood in terms of a general description of transport in Hamiltonian systems in the context of iterations of area-preserving maps. Invariant tori are barriers to the transport but, even when these barriers are absent, there may exist partial barriers constituted by cantori or remnant invariant Cantor sets. The transport through cantori can be explained in terms of turnstiles, which describe the natural transport through gaps between cantori,[38] but a detailed

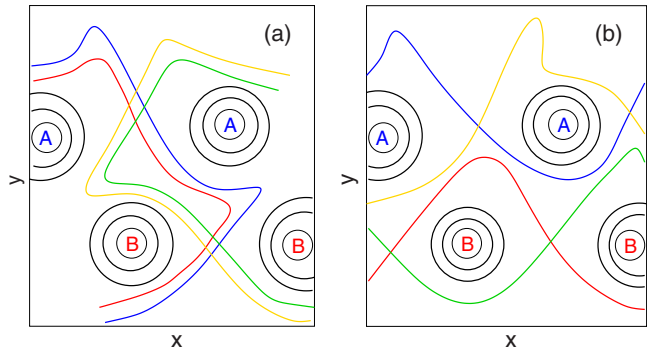

FIG. 11. (Color online) Schematic depiction of (a) both intracrossings and intercrossings and (b) only dominant intracrossings of invariant manifolds of island chains A (up) and B (down) for the SNM.

analysis of this for nontwist systems remains to be done. In the case schematically depicted in Figs. 11(a) and 11(b) we have turnstiles associated with the different kinds of crossings, respectively, where the invariant manifolds can be used to define curves connecting the edges of cantori.

V. CONCLUSIONS

In this work we considered the SNM, a prototype of nontwist system with nonmonotonic shear. A common trait of such systems is the presence of a shearless curve, which constitutes a transport barrier persisting for a wide range of parameter values. Even after the barrier breakdown, the region of the shearless curve continues to reduce transport since the barrier remnants manage to partially trap orbits. Thus, there is an effective barrier if the average trapping time is comparable to the characteristic time scale of interest.

We presented some numerical diagnostics that indicate this trapping effect after the transport barrier is broken. Two of them, the average barrier escape time and the barrier transmissivity, were computed over a parameter range, showing sensitive parameter dependence. Our results can be interpreted using two factors characterizing chaotic orbits in the transport barrier. One factor is the stickiness that traps orbits in the vicinity of periodic islands. For determined parameter values, there is an increase in the trapping time, which is explained by the creation of periodic island subchains of period-3. Thus the evidence presented, and our suggestion that nontwist originates stickiness, is consistent with the fact that generic tripling bifurcations[28] give rise to nontwist behavior.

Another factor influencing the barrier transmissivity is the qualitative change in the nature of the dominant manifold crossings. Since there are two remnant island chains after the transport barrier breakdown, the manifold crossings may be dominated by inter- or intratype. In the former case the barrier transmissivity is higher and the barrier average escape time is lower, while in the latter case the transmissivity is smaller and the average escape time is larger.

ACKNOWLEDGMENTS

This work was made possible by the partial financial support of CNPq, CAPES, FAPESP, and FINEP/CNEN (Brazilian Government Agencies). In addition, P.J.M. was supported by the U.S. Department of Energy (Contract No. DE-FG03-96ER-54346).

[1] J. Moser, Ergod. Theory Dyn. Syst. **6**, 401 (1986).
[2] A. N. Lichtenberg and M. A. Lieberman, *Regular and Chaotic Dynamics*, 2nd ed. (Springer Verlag, Berlin, 1992).
[3] B. V. Chirikov, Phys. Rep. **52**, 263 (1979).
[4] D. Del-Castillo-Negrete and P. J. Morrison, Phys. Fluids A **5**, 948 (1993).
[5] D. Del-Castillo-Negrete, J. M. Greene, and P. J. Morrison, Physica D **91**, 1 (1996).
[6] D. Del-Castillo-Negrete, J. M. Greene, and P. J. Morrison, Physica D **100**, 311 (1997).
[7] D. Del-Castillo-Negrete and P. J. Morrison, in *Chaotic Dynamics and Transport in Fluids and Plasmas*, Research Trends in Physics, edited by I. Prigogine (American Institute of Physics, New York, 1992), p. 181.
[8] W. Kerner and H. Tasso, Phys. Rev. Lett. **49**, 654 (1982).
[9] M. G. Davidson, R. L. Dewar, H. J. Gardner, and J. Howard, Aust. J. Phys. **48**, 871 (1995).
[10] M. P. Bernardin and J. A. Tataronis, J. Math. Phys. **26**, 2370 (1985).
[11] P. J. Morrison, Rev. Mod. Phys. **70**, 467 (1998); Phys. Plasmas **7**, 2279 (2000).
[12] E. Mazzucato, S. H. Batha, M. Beer, M. Bell, R. E. Bell, R. V. Budny, C. Bush, T. S. Hahm, G. W. Hammett, F. M. Levinton, R. Nazikian, H. Park, G. Rewoldt, G. L. Schmidt, E. J. Synakowski, W. M. Tang, G. Taylor, and M. C. Zarnstorff, Phys. Rev. Lett. **77**, 3145 (1996).
[13] D. Del-Castillo-Negrete and P. J. Morrison, Bull. Am. Phys. Soc. **37**, 1547 (1992).
[14] W. Horton, H. B. Park, J. M. Kwon, D. Strozzi, P. J. Morrison, and D. I. Choi, Phys. Plasmas **5**, 3910 (1998).
[15] E. C. da Silva, I. L. Caldas, and R. L. Viana, IEEE Trans. Plasma Sci. **29**, 617 (2001).
[16] G. A. Oda and I. L. Caldas, Chaos, Solitons Fractals **5**, 15 (1995); G. Corso and A. J. Lichtenberg, Physica D **131**, 1 (1999).
[17] D. Del-Castillo-Negrete, Phys. Plasmas **7**, 1702 (2000).
[18] F. A. Marcus, T. Kroetz, M. Roberto, I. L. Caldas, E. C. da Silva, R. L. Viana, and Z. O. Guimarães-Filho, Nucl. Fusion **48**, 024108 (2008).
[19] F. A. Marcus, I. L. Caldas, Z. O. Guimarães-Filho, P. J. Morrison, W. Horton, Yu. K. Kuznetsov, and I. C. Nascimento, Phys. Plasmas **15**, 112304 (2008).
[20] M. Jakubowski, S. S. Abdullaev, K. H. Finken, M. Lehnen, and the TEXTOR Team, J. Nucl. Mater. **532**, 337 (2005).
[21] A. Wingen, M. Jakubowski, K. H. Spatschek, S. S. Abdullaev, K. H. Finken, and A. Lehnen, Phys. Plasmas **14**, 042502 (2007).
[22] T. E. Evans, I. Joseph, R. A. Moyer, M. E. Fenstermacher, C. J. Lasnler, and L. W. Yan, J. Nucl. Mater. **363–365**, 570 (2007).
[23] A. Wurm, A. Apte, and P. J. Morrison, Braz. J. Phys. **34**, 1700 (2004).
[24] A. Wurm, A. Apte, K. Fuchss, and P. J. Morrison, Chaos **15**, 023108 (2005).
[25] S. Aubry and P. Y. LeDaeron, Physica D **8**, 381 (1983); J. N. Mather, Topology **21**, 457 (1982); R. S. MacKay, Nonlinearity **5**, 161 (1992).
[26] A. Delshams and R. de la Llave, SIAM J. Math. Anal. **31**, 1235 (2000).
[27] C. Simo, Regular Chaotic Dyn. **3**, 180 (1998).
[28] H. R. Dullin, J. D. Meiss, and D. Sterling, Nonlinearity **13**, 203 (2000).
[29] K. Ullmann and I. L. Caldas, Chaos, Solitons Fractals **11**, 2129 (2000).
[30] J. D. Meiss and E. Ott, Phys. Rev. Lett. **55**, 2741 (1985); G. Zaslavsky and M. Edelman, Chaos **10**, 135 (2000).
[31] D. Del-Castillo-Negrete, B. A. Carreras, and V. E. Lynch, Phys. Plasmas **11**, 3854 (2004).
[32] J. D. Szezech, Jr., S. R. Lopes, and R. L. Viana, Phys. Lett. A **335**, 394 (2005).
[33] E. Ott, *Chaos in Dynamical Systems* (Cambridge University Press, Cambridge, England, 1993).
[34] G. Corso and F. B. Rizzato, Phys. Rev. E **58**, 8013 (1998).
[35] T. E. Evans, R. A. Moyer, and P. Monat, Phys. Plasmas **9**, 4957 (2002).
[36] H. Kantz and P. Grassberger, Physica D **17**, 75 (1985).
[37] J. S. E. Portela, I. L. Caldas, R. L. Viana, and M. A. F. Sanjuán, Int. J. Bifurcation Chaos Appl. Sci. Eng. **17**, 4067 (2007).
[38] R. S. MacKay, J. D. Meiss, and I. C. Percival, Physica D **13**, 55 (1984).